JOURNAL OF Materials CHEMISTRY

Preparation and porous texture characteristics of fibrous ultrahigh surface area carbons†

Fabián Suárez-García, Juan I. Paredes, Amelia Martínez-Alonso and Juan M. D. Tascón*

Instituto Nacional del Carbón, CSIC, Apartado 73, 33080 Oviedo, Spain. E-mail: tascon@incar.csic.es

Received 26th April 2002, Accepted 17th May 2002
First published as an Advance Article on the web 3rd October 2002

Microporous carbon adsorbents with fibrous morphology and very high surface area and pore volume development were prepared from poly (*m*-phenylene isophthalamide) fibres. The precursor polymer was impregnated with aqueous solutions of phosphoric acid, carbonised and physically activated with CO_2 to different burn-off degrees. The char yield following pyrolysis increased with the impregnation ratio. Additionally, pre-impregnation with phosphoric acid strongly enhanced the reactivity of chars towards CO_2, there being a positive correlation between reactivity, impregnation ratio and oxygen content in the chars. The porous texture of the obtained materials was characterized by physical adsorption of N_2 at 77 K and CO_2 at 273 K. The pores enlarged slightly with increasing burn-off in CO_2, though remaining restricted to the micropore region. No pores larger than 3–4 nm were ever found in any of the activated materials, even at high burn-offs. Ultrahigh surface area carbons with BET surface areas over 2000 $m^2\ g^{-1}$ and pore volumes in excess of 1.10 $cm^3\ g^{-1}$ were obtained at high burn-offs, displaying an extensive network of supermicropores considerably wider than those obtained under equivalent conditions in the absence of the H_3PO_4 additive. To complement these observations, scanning tunneling microscopy was performed on the ultrahigh surface area carbons. Visual evidence was provided of an extensive network of $\sim$2 nm pores, consistent with the physical adsorption measurements.

1. Introduction

Activated carbons (ACs) have found widespread utilisation in different fields such as gas storage, separation of mixtures, catalysis and, especially, environmental applications.[1] This is facilitated by the versatility of this class of porous materials, which can be produced with different adsorption capacities, these being determined in turn by their porous texture and surface functionalities. Recent reports show that ultrahigh surface area carbons, having surface areas over 2000 $m^2\ g^{-1}$ and pore volumes in excess of 1 $cm^3\ g^{-1}$, can be prepared from different types of precursors: pitch,[2] petroleum coke,[3] coal,[4,5] lignocellulosic materials,[6,7] polymers,[8–10] *etc.* To date, approaches to prepare ultrahigh surface area carbons consist of a combination of physical and chemical activations in the case of lignocellulosic precursors,[6,7] or chemical activation with KOH for other types of precursors.[2–5,8,10]

Activated carbon fibres (ACFs), *i.e.*, activated carbons with fibrous morphology, offer a number of advantages over conventional (granular or powdered) ACs. Thus, ACFs exhibit higher adsorption/desorption rates, narrower pore size distributions, are easy to handle, can be molded, have no packing or channelling problems and can be used in the form of cloth, paper, felt, *etc.* ACFs are typically prepared from low-crystallinity fibrous precursors such as poly(acrylonitrile), cellulose, phenolic resin, pitch, viscose rayon, *etc.*[11]

The use of high-crystallinity fibrous polymers such as Kevlar [poly(*p*-phenylene terephthalamide)] and Nomex [poly(*m*-phenylene isophthalamide)] as precursors for ACFs was initially proposed by Freeman *et al.*[12,13] In our laboratory, ACFs have been prepared from these two precursors by physical activation with CO_2,[14,15] a particularly interesting feature of these adsorbents being a very narrow pore size distribution in the micropore region. Nomex leads to a higher homogeneity in pore size than Kevlar, yielding adsorbents with practically no mesopores, even at high burn-offs. However, a practical disadvantage of Nomex chars is a lower reactivity for CO_2 activation in comparison with Kevlar chars.

In this work we report on the advantages of Nomex impregnation with phosphoric acid as a pre-treatment leading to fibrous, ultrahigh surface area carbons. Moreover, it will be shown that this impregnation results in an increase in the pyrolysis yield as well as a higher reaction rate of chars during their subsequent activation in CO_2.

2. Experimental

2.1. Preparation of ACFs

The starting material was crystalline Nomex *tow*, 2.2 dtf (decitex per filament). Various series of carbon adsorbents were prepared from either fresh Nomex (N), or Nomex pre-impregnated with different amounts of H_3PO_4 (NP). The impregnation process was carried out in a rotary evaporator, using each time 10 g Nomex and 200 ml of a solution of phosphoric acid of different concentration to get different impregnation ratios in the product. The temperature was increased progressively while stirring until evaporation of excess water was complete; this process lasted for 6 h. Then, the samples were dried in a vacuum furnace at 383 K. The impregnation ratio [calculated as the weight gain after impregnation relative to the initial mass of Nomex, *i.e.* (g H_3PO_4/g Nomex) $\times$ 100] amounted to 1, 3, 7 and 9 wt.%; the resulting samples have been named NP1, NP3, NP7 and NP9, respectively.

Pyrolysis/activation of fresh or impregnated Nomex was carried out in a vertical quartz reactor, using 4–5 g of Nomex and an argon (99.999% pure) flow of 50 $cm^3\ min^{-1}$. The

†Basis of a presentation given at Materials Discussion No. 5, 22–25 September 2002, Madrid, Spain.

pyrolysis was programmed at a heating rate of 10 K min^{-1} to a maximum temperature of 1123 K; once this temperature was attained, the sample was cooled down at 10 K min^{-1} to 1073 K and kept at this temperature for 10 min. Then, the gas flow was changed to 50 cm^3 min^{-1} CO_2 (99.98% pure), and it was kept for different time intervals to attain different burn-off (BO) degrees. Once the activation step was finished, the samples were cooled down to room temperature under an Ar flow of 50 cm^3 min^{-1}.

After having completed the pyrolysis/activation step of Nomex impregnated with phosphoric acid, the residues were washed with water in a Soxhlet extractor to eliminate the excess of phosphoric acid and/or its descomposition products until the conductivity in the washing liquids was <3 μS cm^{-1} (measured with a pH/conductivity meter, Mettler Toledo, model MPC227). After washing, the samples were dried for 12 hours at 383 K under vacuum.

The yield and the BO of samples prepared from pre-impregnated Nomex were calculated from the final mass (after washing and drying) relative to the initial mass of Nomex before impregnation. Materials studied in this work are identified as N-BO for the series of samples prepared from fresh, non-impregnated Nomex, and as NP-impregnation ratio-BO for those prepared from pre-impregnated Nomex. Thus, N-25 is an ACF obtained from fresh Nomex pyrolyzed and then activated in CO_2 to 25% BO, whereas NP9-65 is an ACF obtained from Nomex impregnated with 9 wt.% phosphoric acid and activated in CO_2 to 65% BO.

2.2. Characterisation techniques

Elemental analyses of chars (N-0, NP1-0, NP3-0, NP7-0, NP9-0) were carried out in a microanalysis apparatus, LECO CHNS-932, provided with an oxygen analyzer, LECO VTF-900. X-ray diffractograms of the same materials were obtained in a Siemens D5000 diffractometer using Cu Kα radiation ($\lambda =$ 0.15406 nm) at a step size of 0.015° and step time of 3 s. The mass loss of the same samples between room temperature and 1273 K was studied in a Stanton-Redcroft STA-1500 thermobalance, using 15 mg sample, a heating rate of 10 K min^{-1} and an Ar flow of 50 cm^3 min^{-1}.

The porous texture of samples was analyzed from physical adsorption isotherms of N_2 (99.999% pure) at 77 K, measured in an automatic volumetric adsorption apparatus, ASAP 2010 (Micromeritics) and CO_2 (99.98% pure) at 273 K, measured in a semiautomatic volumetric adsorption apparatus, NOVA 1200 (Quantachrome). Porous texture parameters obtained from the N_2 isotherms were: the BET surface area, S_{BET}, calculated according to the BET model; the micropore volume, $V_{\mu p}$ (DR, N_2), by means of the Dubinin-Radushkevich (DR) equation; the external (or non-microporous) surface area, S_{ext} (α_S), the ultramicropore volume, $V_{u\mu p}$ (α_S) and the total micropore volume, $V_{\mu p}$ (α_S), following the α_S method as proposed by Gregg and Sing[16] (using Spheron 6 carbon black as reference); and the specific surface area, a_s (α_S), applying the revision of the α_S method for high-resolution isotherms proposed by Kaneko *et al.*[17] The DFT method was employed to obtain the pore size distribution and the ultramicropore volume, $V_{u\mu p}$ (DFT), the total micropore volume, $V_{\mu p}$ (DFT) and the mesopore volume, V_{mp} (DFT). The total pore volume, V_t, was calculated from the amount of N_2 adsorbed at a relative pressure of 0.975, assuming it to be adsorbed in liquid form (Gurvitsch rule). The CO_2 adsorption isotherms were analyzed according to the DR method to determine the micropore volume, $V_{\mu p}$ (DR, CO_2) and the micropore equivalent surface area, $S_{\mu p}$ (DR, CO_2).

As a complement to the physical adsorption measurements, scanning tunneling microscopy (STM) imaging of the super-activated carbon fibres was performed with the aim of gathering visual evidence of their porous structure. STM has been very recently employed for the characterisation of activated carbon materials[18,19] where the high resolution capabilities of the technique were able to reveal the micro- and mesoporosity present in this type of sample. STM imaging was performed in air at room temperature with a Nanoscope Multimode IIIa, from Digital Instruments, using mechanically prepared Pt/Ir (80/20) tips. The images were collected in the constant current mode (variable height). The tunneling parameters typically employed were 600 mV and 0.4 nA for the bias voltage and tunneling current, respectively, although they could be varied along a wide range of values without significant change in the corresponding images. To confirm the reproducibility of the findings, several different and previously unused tips were employed and many different areas of the samples were imaged.

3. Results and discussion

3.1. Yield and reactivity of chars

Table 1 shows the char yields corresponding to pyrolysis of Nomex, alone or impregnated with different amounts of H_3PO_4. As indicated in section 2.1, in the case of samples prepared from impregnated Nomex, the yields were calculated from the mass of char (after washing to eliminate phosphoric acid and/or its decomposition products) and the initial mass of Nomex prior to impregnation. One can see in Table 1 that the char yield increases with increasing impregnation ratio. For impregnation ratios >3 wt.% the corresponding increase in char yield is >10 wt.%. This can be attributed to a modifying effect of H_3PO_4 on the pyrolysis of Nomex, lowering the temperature at which the degradation of the polymer takes place and decreasing the number of decomposition steps, from two for Nomex alone[20] to only one for Nomex pyrolysed in the presence of H_3PO_4.[21] It is believed that the combined effect of these two facts results in the increased char yield; a similar effect has been observed recently with a lignocellulosic precursor for activated carbons.[22]

Fig. 1 shows the evolution of BO as a function of activation time in CO_2 for chars prepared from Nomex, either fresh (N) or impregnated with different amounts of H_3PO_4 (NP1, NP3, NP7, NP9). A linear relationship between BO and time holds for every series of samples. All the series of samples impregnated with phosphoric acid, even at only 1 wt.%, exhibit a slope much larger than that of the N series, indicating a much larger reactivity for the impregnated samples. The reaction rates calculated from the slopes of the straight lines depicted in Fig. 1 are 3.26×10^{-4} g g^{-1} min^{-1} (N series), $1.03 \times$

Table 1 Elemental analysis, structural parameters and pyrolysis yields of Nomex chars

	Elemental analysis (wt.%)						Crystallographic parameters/nm			
Sample	Ash	C	H	N	S	O	d_{002}	L_c	L_a	Yield (wt.%)
N-0	<0.1	83.52	1.47	6.29	—	8.37	0.372	1.1	5.0	52.8
NP1-0	0.3	83.39	0.56	7.13	—	9.59	0.372	1.1	5.2	57.1
NP3-0	0.9	81.33	0.68	6.89	—	11.44	0.379	1.0	6.8	62.7
NP7-0	0.8	80.74	0.58	6.65	—	12.75	0.378	1.1	7.2	64.1
NP9-0	1.2	79.00	0.62	6.36	—	13.72	0.374	1.1	6.2	65.7

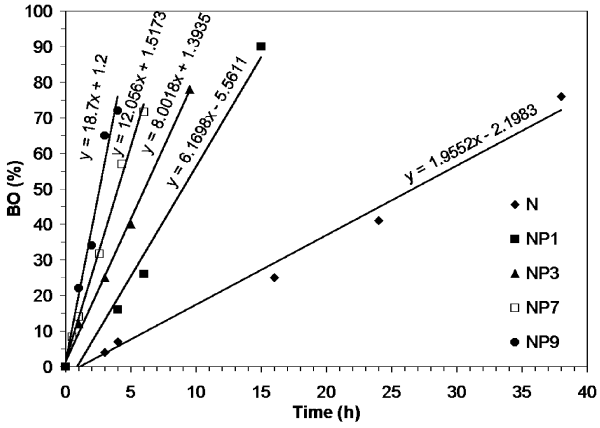

Fig. 1 Variation with time of the burn-off in CO_2 of chars prepared from Nomex, with different impregnation ratios of H_3PO_4 (NP) or not impregnated (N).

10^{-3} g g^{-1} min^{-1} (NP1 series), 1.33 $\times$ 10^{-3} g g^{-1} min^{-1} (NP3 series), 2.01 $\times$ 10^{-3} g g^{-1} min^{-1} (NP7 series) and 3.12 $\times$ 10^{-3} g g^{-1} min^{-1} (NP9 series). Thus, the NP1 series exhibits a reactivity three times larger than the N series, and the reaction rate increases regularly with increasing impregnation ratio, becoming almost one order of magnitude larger (9.6 times) for an impregnation ratio of 9 wt.% (NP9 series).

Various different factors are known to affect the reactivity of carbonaceous solids towards oxidizing gases. These factors can be classified into structural, textural and chemical.[23] Generally speaking, an increase in the degree of structural disorder, in surface area and porosity, and/or in the content of heteroatoms and inorganic impurities, will result in an enhancement in the oxidation reactivity of carbon materials.[23,24] In a preliminary communication,[21] we have characterised samples N-0 and NP-7 in an aim to establish the origin of the difference in reactivity between these two chars. It was concluded that it cannot be attributed to structural and textural factors since parameters accounting for these two types of factors were virtually identical for these two samples. The possible presence of inorganic impurities with catalytic effects could be ruled out as well, and it was also observed that phosphoric acid that is eliminated during the washing step does not participate in the gasification reaction. The remaining explanation for the increase in reactivity was a larger amount of oxygenated functionalities in NP7-0 char relative to N-0 char.

In the current work, the effect of the impregnation ratio on the characteristics of the corresponding Nomex-derived chars has been studied systematically. Table 1 gives crystallographic parameters obtained from X-ray diffractograms. The interlayer spacing (d_{002}), the height (L_c) and the width (L_a) of graphite-like crystallites are similar for all chars; therefore, the difference in reactivity cannot be ascribed to structural factors. In Table 2, porous texture parameters deduced from CO_2 isotherms are given. All the chars adsorb negligible amounts of N_2 at 77 K, exhibiting an S_{BET} of 1 m^2 g^{-1}. However, they adsorb CO_2 at 273 K, exhibiting similar values of $V_{\mu p}$ (DR, CO_2) and $S_{\mu p}$ (DR, CO_2). One can therefore conclude that changing the impregnation ratio of Nomex with H_3PO_4 has no effect on the

Table 2 Textural parameters deduced from CO_2 adsorption at 273 K for Nomex chars (0% BO) with different impregnation ratios

Sample	$S_{\mu p}$ (DR, CO_2)/m^2 g^{-1}	$V_{\mu p}$ (DR, CO_2)/cm^3 g^{-1}
N-0	499	0.18
NP1-0	534	0.19
NP3-0	494	0.18
NP7-0	497	0.18
NP9-0	548	0.20

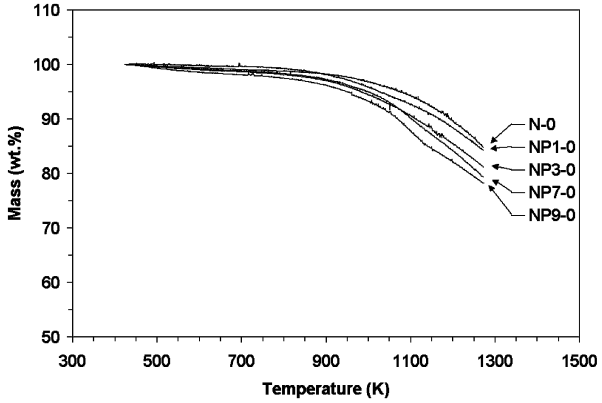

Fig. 2 Mass loss of Nomex chars heated in Ar atmosphere.

porous texture of the corresponding chars, whose reactivities *versus* CO_2 could be expected to be similar on the basis of porous texture.

Table 1 gives elemental analyses of Nomex chars; these materials were washed with water to remove H_3PO_4 and/or its decomposition products following pyrolysis. The oxygen content increases with increasing impregnation ratio following a trend parallel to that of reactivity. We attempted to get additional information on oxygenated groups by studying by thermogravimentry the desorption of surface complexes from the chars. Fig. 2 shows the mass loss of these chars heated from room temperature to 1273 K at 10 K min^{-1} under Ar flow. One can see that the mass loss undergone by the chars increases as the amount of H_3PO_4 used in the impregnation increases. Mass loss of char N-0 begins at 873 K and amounts to 5.2 wt.% (dry basis, db) between this temperature and 1123 K (this is the temperature at which the chars had been pyrolysed). NP1-0 also starts losing mass at 873 K, but it losses 6.7 wt.% (db) up to 1123 K. Mass losses for the rest of chars (NP3-0, NP7-0 and NP9-0) start at a lower temperature (773 K) and amount to 8.9, 10.4 and 11.7 wt.% (db), respectively, between that temperature and 1123 K. According to the temperatures at which mass loss takes place, this can be attributed to elimination of oxygenated functional groups in the form of CO_2 and/or CO. This agrees well with the elemental analyses reported in Table 1 since the mass loss increases with increasing oxygen content. Therefore, in the absence of other (structural, textural or chemical) differences, one can attribute the difference in reactivity to oxygenated functionalities introduced in chars by the effect of phosphoric acid on Nomex pyrolysis.

3.2. Characterisation of the ACFs: adsorption of N_2 and CO_2, STM

Fig. 3 shows adsorption/desorption isotherms of N_2 at 77 K on a selection of ACFs prepared from Nomex, either non-impregnated or impregnated with different impregnation ratios, pyrolysed and then activated with CO_2 to BO $<$ 50%. All the isotherms are type Ia, indicating that pore filling takes place at very low relative pressures in pores of molecular dimensions by primary micropore filling.[25] All of these ACFs are microporous, they do not show evidence of any mesoporosity and, as the shape of the isotherms indicates, they contain an important amount of ultramicropores. As the BO increases, a slight widening in the "knee" of the isotherms takes place (compare, *e.g.*, NP3-40 and N-41 with the rest of the isotherms), indicating that some pore widening takes place. For instance, 97% of the pores in sample NP1-16 are micropores [calculated as the ratio between $V_{\mu p}$ (α_S) and V_t], 65% of which are ultramicropores, *i.e.*, pores smaller than 0.7 nm [calculated as the ratio between $V_{u\mu p}$ (α_S)—data not shown—and $V_{\mu p}$ (α_S)]. However, based on the same criteria, micropores represent 96% of the porosity of sample NP3-40, but only 38% of these are

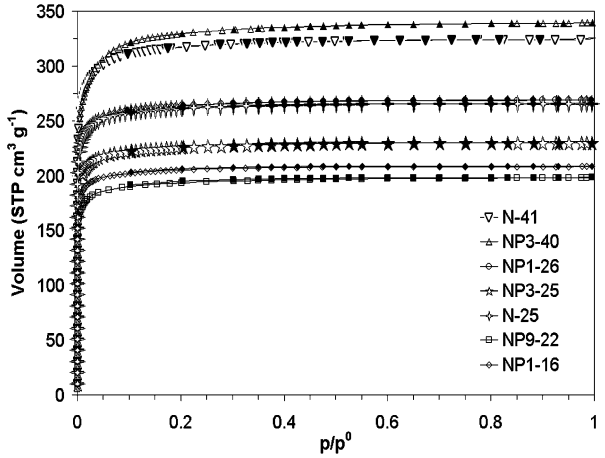

Fig. 3 Adsorption–desorption isotherms of N_2 at 77 K on ACFs from Nomex at BO < 50%. Open symbols: adsorption; full symbols: desorption.

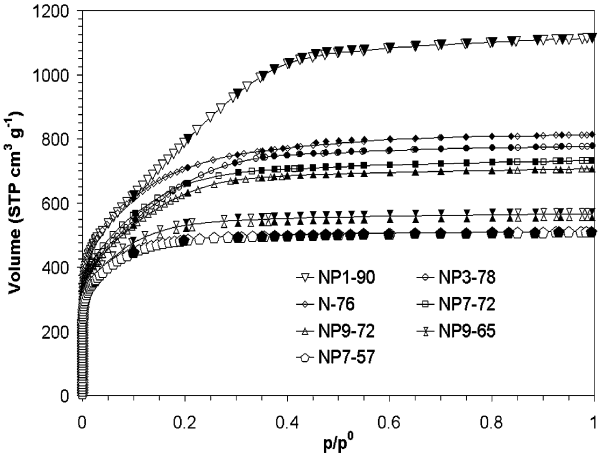

Fig. 4 Adsorption–desorption isotherms of N_2 at 77 K on ACFs from Nomex at BO > 50%. Open symbols: adsorption; full symbols: desorption.

ultramicropores. This decrease in the share of ultramicropores to the total porosity indicates that, although both samples are essentially microporous, the size of micropores increases somewhat upon activation.

The impregnation ratio only affects the porous texture characteristics of materials activated to low BOs where, for a similar BO, the N_2 uptake decreases with increasing impregnation ratio. As Fig. 3 shows, whereas N-25 and NP1-26 yield practically identical N_2 isotherms, the N_2 uptake decreases when the impregnation ratio is increased; thus, NP3-25 and NP9-22 adsorb less N_2 than the two previous samples. A possible reason for this decrease could be that a fraction of phosphoric acid and/or its decomposition products remains in the pores after washing, blocking them. Another possibility would be a different porosity development due to a difference in activation rates, which, as it was shown before, increase with increasing impregnation ratio due to a higher concentration of surface oxygenated functionalities. As a consequence, the impregnated samples would contain a higher amount of active sites at their surface. Therefore, in such samples, reaction with CO_2 at low BOs would be more superficial than for the non-impregnated samples. Consequently, at similar (albeit low) BOs the non-impregnated samples would undergo a greater porosity development.

Unlike the behaviour found at low BOs, differences in porosity development as a function of the impregnation ratio disappear at higher BOs and the samples exhibit similar porosity characteristics as can be deduced from Fig. 3. For instance, samples NP3-40 and N-41 exhibit BET surface areas (S_{BET}) of 1286 m^2 g^{-1} and 1241 m^2 g^{-1}, respectively.

Fig. 4 shows adsorption/desorption isotherms of N_2 at 77 K on ACFs prepared at BO > 50%. These isotherms are type Ib, where the N_2 uptake increases up to relative pressures of 0.2–0.4 (depending on the BO), indicating the presence of wide micropores that are filled by a co-operative filling mechanism.[25] Above this relative pressure, a plateau is attained. Type Ib isotherms such as these are characteristic of high surface area, microporous active carbons, and have been reported by different authors.[4,5,8,26]

In comparing results from Fig. 3 and 4 one can notice that, as the BO increases over the entire range studied, an increase in the amount of adsorbed N_2 takes place in the materials prepared from either non-impregnated Nomex or H_3PO_4-impregnated Nomex. This causes a progressive increase in the BET surface area with increasing BO. Fig. 5, where BET surface areas of samples from the different series are plotted as a function of BO, substantiates more clearly this finding, a practically linear correlation existing between S_{BET} and BO. The surface area developed depends much more on the BO degree than on the amount of H_3PO_4 pre-impregnated on Nomex, or even on the absence or presence of this additive.

Fig. 5 also shows that, already at low BOs, activation with CO_2 is very efficient in opening the narrow microporosity that is present in Nomex chars (as evidenced by CO_2 adsorption, see below). For instance, whereas non-activated chars (0% BO) exhibit BET surface areas of about 1 m^2 g^{-1}, activation to a BO as low as 4% produces ACFs with S_{BET} > 500 m^2 g^{-1}. On the other hand, at BOs > 50%, materials with S_{BET} > 1800 m^2 g^{-1}, are obtained, which grow up to >2800 m^2 g^{-1} for the highest BOs attained.

Working with ultrahigh surface area ACFs, Kaneko *et al.*[17] showed that, depending on the linearity range of fitting N_2 adsorption data to the BET equation, one can greatly overestimate the surface area. To overcome this limitation of the BET method, these authors recommended using their adaptation to high-resolution N_2 adsorption measurements[17] of the α_S method, originally proposed by Gregg and Sing.[16] The high-resolution α_S curves can exhibit two departures from linearity at $\alpha < 1$, designed as filling swing (FS) and cooperative swing (CS), which are due to an enhancement in the surface–molecule interactions as a function of the pore size. The FS phenomenon, associated with the "primary micropore filling" proposed by Gregg and Sing[16] occurs at $\alpha < 0.5$. This phenomenon empirically suggests the presence of ultramicropores, where the interaction between the pseudo-graphitic surface and the adsorbate molecule is strongly enhanced by the overlap with the potential from the opposite pore wall. On the other hand, the CS is attributed to the presence of pores with widths >1.0 nm, where adsorption in the empty space between the

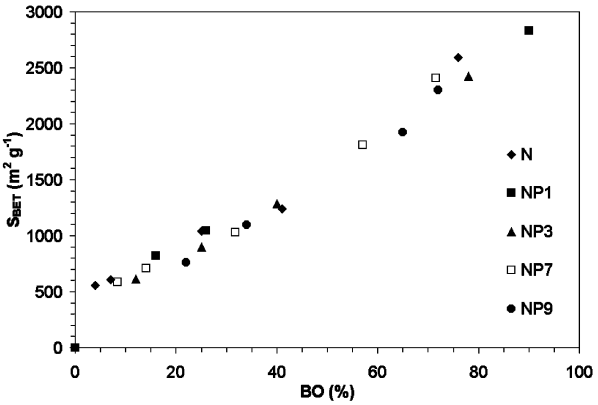

Fig. 5 Variation of the BET surface area with the burn-off degree in CO_2.

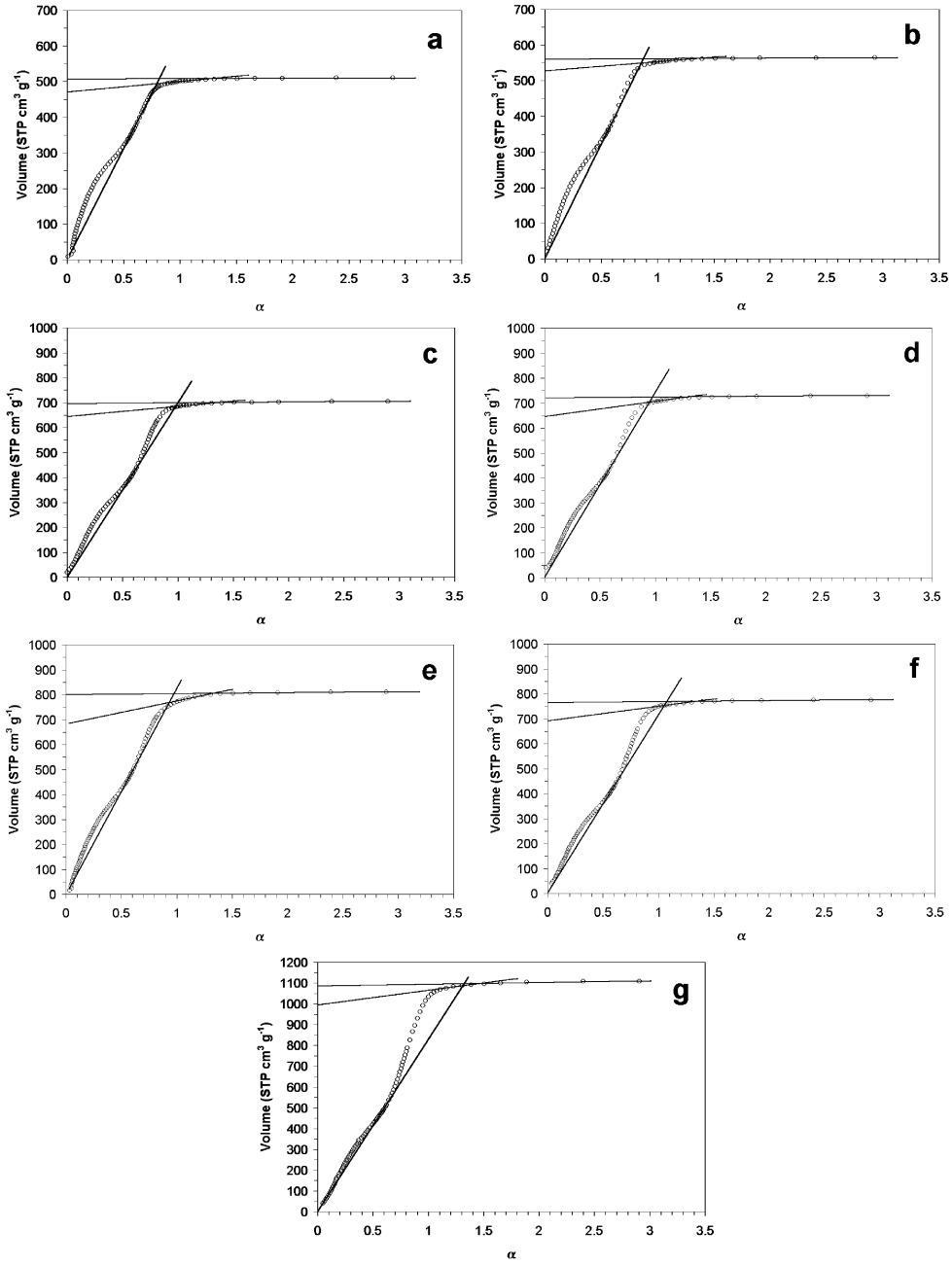

Fig. 6 α_S curves of ACFs with BO > 50%. (a) NP7-57, (b) NP6-65, (c) NP9-72, (d) NP7-72, (e) N-76, (f) NP3-78 and (g) NP1-90.

monolayer adsorbed on the pore wall is, presumably, accelerated regarding multilayer adsorption on the flat surface. CS is frequently observed at $\alpha > 0.7$ in high surface area activated carbons, being responsible for the overestimation of the surface area when calculated by the BET method.[17]

Fig. 6 shows α_S curves corresponding to ACFs with BOs > 50%. The reference material used in this work was Spheron 6 carbon black, which yields a type II N_2 isotherm, making possible the calculation of a reliable surface area by the BET method; a value of 109 m^2 g^{-1} was obtained. For the ACFs obtained at the lowest BOs, namely 57 and 65% (Fig. 6 a–b), deviations at $\alpha < 0.5$ due to FS are observed, indicating the presence of small micropores with a width < 1.0 nm. As the BO increases (Fig. 6 c–g), one observes the presence of departures from linearity for $\alpha < 0.5$ and $\alpha > 0.7$, due to FS and CS, respectively, although the FS progressively decreases as the BO increases, and practically disappears for the sample with 90% BO (Fig. 6g). The presence of both types of deviation suggests that these samples contain both narrow micropores (ultramicropores) and wide micropores (supermicropores).

Different possible fitting straight lines are shown on Fig. 6. From the slope of the line fitting values of $\alpha > 1.5$, the external or non-microporous surface, S_{ext} (α_S), can be obtained. From the intercept of the straight line fitting values of $\alpha > 1$ one can calculate the micropore volume, $V_{\mu p}$ (α_S). The third line drawn fits values of $0.5 < \alpha < 0.7$, goes through the origin of coordinates, and from its slope one can calculate the true surface area, a_S (α_S), as proposed by Kaneko *et al.* by means of the subtracting pore effect (SPE) method.[17]

Table 3 gives the yields and a number of textural parameters deduced from the adsorption isotherms of N_2 at 77 K and CO_2 at 273 K, for ACFs obtained at BOs > 50%. The S_{BET} is always larger than a_S (α_S), confirming that for these materials the BET method overestimates the true specific surface area. It can be observed that, for the two samples with BOs < 70%, the difference between these two parameters is small; correspondingly, these two samples do not exhibit CS (see Fig. 6 a,b). However, the difference between S_{BET} and a_S (α_S) becomes larger with increasing BO as a consequence of the CS (see Fig. 6 c–g), in agreement with Kaneko *et al.*[17] The samples activated

Table 3 Textural parameters deduced from N_2 and CO_2 isotherms. Surface areas in $m^2\ g^{-1}$; volumes in $cm^3\ g^{-1}$

		N_2									CO_2
Sample	Yield (wt.%)	S_{BET}	a_S (α_S)	S_{ext} (α_S)	V_t	$V_{\mu p}$ (DR)	$V_{\mu p}$ (α_S)	$V_{u\mu p}$ (DFT)	$V_{\mu p}$ (DFT)	V_{mp} (DFT)	$V_{\mu p}$ (DR)
NP7-57	27	1809	1784	4	0.79	0.75	0.74	0.12	0.57	0.08	0.38
NP9-65	23	1925	1848	5	0.87	0.80	0.81	0.12	0.59	0.14	0.38
NP9-72	18	2303	2008	9	1.09	1.02	1.00	0.11	0.59	0.33	0.38
NP7-72	18	2408	2136	11	1.13	1.00	1.00	0.12	0.65	0.30	0.38
N-76	12	2592	2370	11	1.26	1.13	1.02	0.12	0.72	0.35	0.44
NP3-78	15	2425	2090	11	1.20	1.04	1.08	0.12	0.58	0.45	0.40
NP1-90	6	2832	2386	25	1.72	1.21	1.54	0.10	0.53	0.97	0.45

to the highest BOs exhibit a_S (α_S) values $>2000\ m^2\ g^{-1}$ and pore volumes $V_t > 1.10\ cm^3\ g^{-1}$.

Table 3 also indicates that the micropore volumes, $V_{\mu p}$ (DR, N_2) and $V_{\mu p}$ (α_S), of the materials activated to the highest BOs are very high and close to the total pore volume calculated by the Gurvitsch rule from the uptake at relative pressures near unity. This confirms that these samples are essentially microporous, as could be expected from the shape of their isotherms (type Ib, Fig. 4); accordingly, these materials exhibit low external (or non-microporous) surfaces, S_{ext} (α_S), between 4 and 25 $m^2\ g^{-1}$. On the other hand, although their micropore volumes as calculated from CO_2 adsorption [$V_{\mu p}$ (DR, CO_2)] are high, they are considerably smaller than those calculated from the N_2 isotherms [$V_{\mu p}$ (DR, N_2) and $V_{\mu p}$ (α_S)]. This evidences the presence of wide micropores that are not filled with CO_2 at 273 K due to the low relative pressures attained (maximum, 0.035 at 273 K); under these conditions, CO_2 is known to measure only narrow microporosity.

Fig. 7 shows the pore size distributions (PSDs) of various ACFs as deduced from the DFT method. All the samples systematically exhibit a minimum at around 1 nm, which is known to be an artefact introduced by modelling assumptions.[27] All the studied ACFs exhibit PSDs going from ultramicropores to supermicropores or small mesopores (only for the highest BOs). Two maxima appear in all cases, one of them

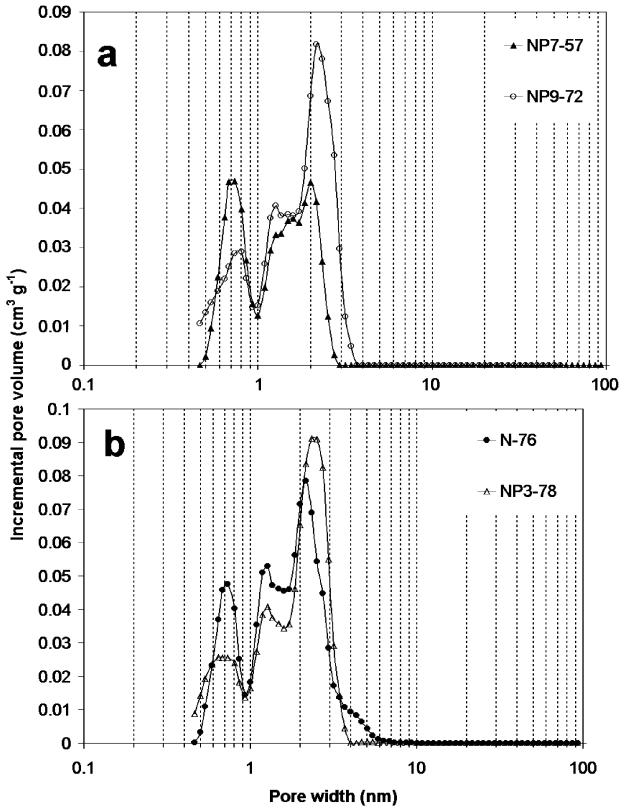

Fig. 7 PSDs calculated by the DFT method for selected ACF samples.

around 0.7 nm and the other between 2 and 2.3 nm (except for NP1-90, where it appears at 2.7 nm; result not shown). The first maximum is responsible for the FS observed in the α_S curves, whereas the second one would account for the CS process (see Fig. 6). As the BO increases the first maximum decreases in intensity whereas the second maximum increases together with a slight displacement towards pores of larger size (from 2 to 2.3–2.7 nm).

Table 3 reports values of different pore volume-related parameters as calculated from the DFT results. The ultramicropore volume, $V_{u\mu p}$ (DFT), was calculated as the cumulative volume of pores <0.7 nm, the micropore volume $V_{\mu p}$ (DFT) as the volume of pores <2 nm and the mesopore volume V_{mp} (DFT) as the volume of pores between 2–50 nm. Neither of the studied samples has pores >4 nm, in agreement with their low external surface areas.

In examining results from Table 3 one can notice that $V_{u\mu p}$ (DFT) remains nearly constant at 0.12 $cm^3\ g^{-1}$ whereas the micropore and total pore volumes increase with increasing BO. Therefore, the contribution of ultramicropores to the porosity of these materials decreases with increasing BO. On the other hand, V_{mp} (DFT) increases with increasing BO (let us remember here that no mesopores >4 nm were found in any sample), but $V_{\mu p}$ (DFT) increases much less, and goes through a maximum for ACF N-76. This shows that, as the BO increases during activation with CO_2, new pores are created [constancy of $V_{u\mu p}$ (DFT)], and the existing micropores are widened [increase in V_{mp} (DFT)]. In comparing samples N-76 and NP3-78 (see Table 3 and Fig. 7b), it can be noticed that the ACF prepared in the absence of phosphoric acid (N-76) exhibits smaller pore sizes, a larger micropore volume and a smaller mesopore volume than NP3-78. This indicates that, when activation is carried out in the presence of H_3PO_4, widening of pre-existing pores occurs to a larger extent than in the absence of H_3PO_4.

Finally, Fig. 8 presents some STM images revealing the nanometer-scale structure of one of the typical ultrahigh surface area carbon fibres prepared in this work (specifically, NP9-72). One of the most prominent characteristics of the fibre surface is its high degree of structural homogeneity. Specifically, the general appearance of virtually all the areas examined was the same as that shown in Fig. 8a, where a large number of minute features, or platelets, with lateral sizes ranging typically between 2 and 5 nm, spread all over the fiber surface. It is also noticed from the image of Fig. 8a that no mesopores (*i.e.* pores significantly larger than 2 nm but less than 50 nm in size) are present on the fiber surface, this being consistent with the absence of hysteresis in the N_2 (77 K) adsorption/desorption isotherms of this sample (Fig. 4) and with the PSDs obtained by the DFT method (Fig. 7), where no pores larger than 4 nm were found. On the other hand, narrow grooves were observed in between the platelets. This can be appreciated with more detail in Fig. 8b, where a more or less interconnected network of deep and winding channels separating the platelets is apparent. The channels are typically between 1.5 and 2.5 nm wide, although narrower channels (*e.g.*, of about 1 nm) were also detected. In some cases, isolated channels or even rounded

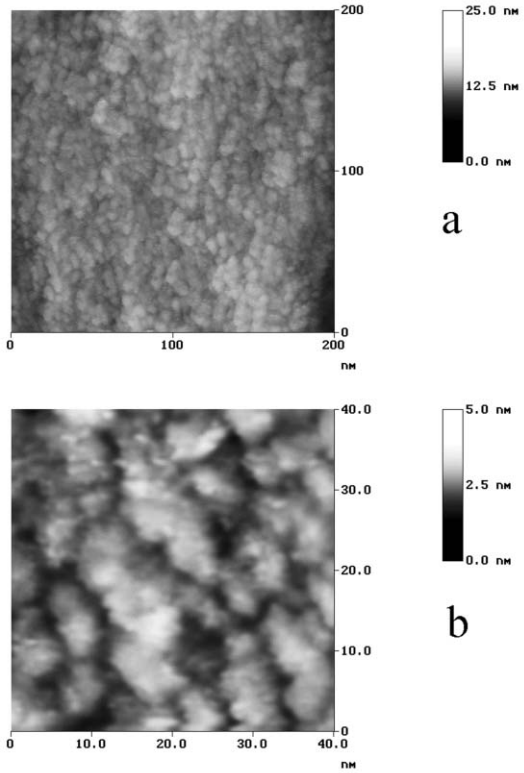

Fig. 8 Typical STM images of NP9-72 sample. (a) General appearance on the nanometer scale. (b) Detailed image showing extensive networks of micropores.

holes with similar widths/diameters to those mentioned previously were observed instead. Taking into account that (1) the deep and interconnected channels/holes found here were never encountered on the STM images of non-activated carbon fibres (0% BO) prepared from Nomex,[18] and (2) the range of channel widths/hole diameters measured in the present STM images is in reasonable agreement with the range of pore sizes deduced from the physical adsorption measurements, we conclude that the channels/holes discerned in the images (Fig. 8b) are the micropores developed in the ultrahigh surface area carbon fibres. Furthermore, we believe that it is such ultrafine structure of platelets, and the very large density of voids (micropores) that it gives rise to in between, that are ultimately responsible for the extremely high adsorptive capability of these samples.

4. Conclusions

The addition of phosphoric acid has been shown to provide a two-fold advantageous effect in the pyrolysis and activation of Nomex with CO_2. First, it alters the mechanism of Nomex pyrolysis, leading to an increase in yield. Second, the resulting chars possess a reactivity higher than that of the char pyrolyzed in the absence of phosphoric acid. Both yield and reactivity follow the same trend, that is, they increase with the impregnation ratio. The increase in yield was attributed to a lowering in the temperature at which degradation of the polymer takes place and a reduction in the number of decomposition steps. The origin of the increase in reactivity was attributed to the higher concentration of oxygenated groups in chars pre-impregnated with phosphoric acid. It was observed that the concentration of such groups and the reactivity followed the same trend as the impregnation ratio was varied.

The development of a porous texture in ACFs depends mainly on the BO degree rather than on the presence of the additive. The pore size was observed to increase slightly with increasing BO in CO_2, but remained restricted to the micropore region. For BO degrees larger than 70%, ACFs with specific surface areas [a_S (α_S)] and pore volumes larger than 2000 $m^2\ g^{-1}$ and 1.10 $cm^3\ g^{-1}$, respectively, were obtained. Finally, STM imaging of the ultrahigh surface area carbon fibres showed evidence of an extensive network of $\sim$2 nm-wide pores, in agreement with the physical adsorption results.

Acknowledgement

Financial support from CICYT (project 1FD1997-1915) is gratefully acknowledged.

References

1 F. Derbyshire, M. Jagtoyen, R. Andrews, A. Rao, I. Martín-Gullón and E. A. Grulke, in *Chemistry and Physics of Carbon*, ed. L. R. Radovic, Marcel Dekker, New York, 2001, vol. 27, pp. 1–66.
2 W. Qiao, L. Ling, Q. Zha and L. Liu, *J. Mater. Sci.*, 1997, **32**, 4447–4453.
3 T. Otawa, Y. Nojima and T. Miyazaki, *Carbon*, 1997, **35**, 1315–1319.
4 Y. Zou and B-X. Han, *Energy & Fuels*, 2001, **15**, 1383–1386.
5 D. Lozano-Castelló, M. A. Lillo-Ródanas, D. Cazorla-Amarós and A. Linares-Solano, *Carbon*, 2001, **39**, 741–749.
6 M. Molina-Sabio, F. Rodríguez-Reinoso, F. Caturla and M. J. Sellés, *Carbon*, 1996, **34**, 457–462.
7 Z. Hu and M. P. Srinivasan, *Microporous Mesoporous Mater.*, 2001, **43**, 267–275.
8 Z. Ryu, J. Zheng, M. Wang and B. Zhang, *J. Colloid Interface Sci.*, 2000, **230**, 312–319.
9 S. Y. You, Y. H. Park and C. R. Park, *Carbon*, 2000, **38**, 1453–1460.
10 A-H. Lu and J-T. Zheng, *J. Colloid Interface Sci.*, 2001, **236**, 369–374.
11 N. M. Osmond, *Adsorption Sci. Technol.*, 2000, **18**, 529–539.
12 J. J. Freeman, J. B. Tomlinson, K. S. W. Sing and C. R. Theocharis, *Carbon*, 1993, **31**, 865–869.
13 J. J. Freeman, J. B. Tomlinson, K. S. W. Sing and C. R. Theocharis, *Carbon*, 1995, **33**, 795–799.
14 A. Martínez-Alonso, M. Jamond, M. A. Montes-Morán and J. M. D. Tascón, *Microporous Mater.*, 1997, **11**, 303–311.
15 M. C. Blanco López, A. Martínez-Alonso and J. M. D. Tascón, *Microporous Mesoporous Mater.*, 2000, **34**, 171–179.
16 S. J. Gregg and K. S. W. Sing, in *Adsorption, Surface area and Porosity*, Academic Press, London, 1982.
17 K. Kaneko, C. Ishii, M. Ruike and H. Kuwabara, *Carbon*, 1992, **30**, 1075–1088.
18 J. I. Paredes, A. Martínez-Alonso and J. M. D. Tascón, *Langmuir*, 2001, **17**, 474–480.
19 P. Pfeifer, F. Ehrburger-Dolle, T. P. Reiker, M. T. González, W. P. Hoffman, M. Molina-Sabio, F. Rodríguez-Reinoso, P. W. Schmidt and D. J. Voss, *Phys. Rev. Lett.*, 2002, **88**, 115502.
20 S. Villar-Rodil, A. Martínez-Alonso and J. M. D. Tascón, *J. Anal. Appl. Pyrolysis*, 2001, **58–59**, 105–115.
21 F. Suárez-García, A. Martínez-Alonso and J. M. D. Tascón, *Fuel Process. Technol.*, 2002, **77–78**, 237–244.
22 F. Suárez-García, A. Martínez-Alonso and J. M. D. Tascón, *J. Anal. Appl. Pyrolysis*, 2002, **62**, 93–109.
23 A. Martínez-Alonso and J. M. D. Tascón, in *Fundamental Issues in Control of Carbon Gasification Reactivity*, ed. J. Lahaye and P. Ehrburger, Kluwer, Dordrecht, 1991, p. 435.
24 H. Marsh and K. Kuo, in *Introduction to Carbon Science*, ed. H. Marsh, Butterworths & Co., London, 1989, p. 107.
25 F. Rouquerol, J. Rouquerol and K. S. W. Sing, in *Adsorption by Powders and Porous Solids. Principles, Methods and Applications*, Academic Press, San Diego, CA, 1999.
26 H. Teng and S-C. Wang, *Carbon*, 2000, **38**, 817–824.
27 J. P. Olivier, *Carbon*, 1998, **36**, 1469–1472.